JOURNAL OF AIRCRAFT
Vol. 40, No. 1, January–February 2003

Performance and Stability of Ducted-Fan Uninhabited Aerial Vehicle Model

Giulio Avanzini* and Salvatore D'Angelo†
Politecnico di Torino, 10129 Turin, Italy
and
Guido de Matteis‡
University of Rome "La Sapienza," 00184 Rome, Italy

The nonlinear model of a novel ducted-fan uninhabited aerial vehicle is presented, where the aerodynamic coefficients are determined by numerical analysis of the flowfield about the airframe. The model is used to investigate performance and stability characteristics and to gain a sound physical understanding of dynamic behavior of this unconventional design. Finally, the influence of uncertainty in the aerodynamic derivatives on the open-loop dynamics is discussed as a result of significant approximations in the aerodynamic analysis.

Nomenclature

$\boldsymbol{A}$	=	state matrix
C_H, C_T, C_Y	=	rotor drag, thrust and sideforce coefficients
C_l, C_m	=	rotor roll and pitch moment coefficients
C_Q	=	rotor torque coefficient
D_f, C_f, L_f	=	force components on the fuselage in wind axes
d_f	=	airframe external diameter
$\boldsymbol{F}$	=	force vector
$\boldsymbol{G}$	=	moment vector
g	=	gravity acceleration
J_x, J_y, J_z	=	moments of inertia
J_{xz}	=	product of inertia
L, M, N	=	moment components
$\boldsymbol{L}_{BI}, \boldsymbol{L}_{BW}$	=	transformation matrices
l_f, m_f, n_f	=	moment components on the airframe in wind axes
m	=	mass
P_R	=	required power
R	=	rotor radius
$\boldsymbol{r}$	=	position vector
S_f	=	fuselage reference area
$\boldsymbol{u}$	=	control vector
V	=	velocity modulus
$\boldsymbol{v}_c$	=	$(u, v, w)^T$ velocity vector
v_i	=	induced velocity
X, Y, Z	=	force components in body axes
$\boldsymbol{x}$	=	state vector
α	=	angle of attack
β_x	=	sideslip angle
δ_A	=	lateral cyclic input, positive right
δ_B	=	longitudinal cyclic input, positive after
δ_C	=	collective control input, positive up
δ_P	=	differential collective, positive right
ρ	=	air density
τ	=	time constant
$\boldsymbol{\Phi}$	=	$(\phi, \theta, \psi)^T$ Euler angle vector
Ω	=	rotor speed
$\boldsymbol{\omega}$	=	$(p, q, r)^T$ angular velocity vector

Subscripts

A	=	airframe
f	=	fuselage
l	=	lower rotor
R	=	rotor
u	=	upper rotor

Received 28 January 2002; revision received 1 September 2002; accepted for publication 25 September 2002.

*Research Scientist, Department of Aerospace Engineering.
†Associate Professor, Department of Aerospace Engineering.
‡Professor, Department of Mechanics and Aeronautics. Member AIAA.

I. Introduction

THE rotary-wing uninhabited aerial vehicle (UAV) shown in Fig. 1, has been designed and is currently being constructed at the University of Rome "La Sapienza" and Politecnico di Torino to be used as a test bench for basic research in applied aerodynamics and flight control systems.

The feasibility of a ducted (or shrouded) configuration involving a moderate forward tilt in crusing flight, the first applications of which were proposed in the late 1950s, has been successfully demonstrated in the industry by the Sikorsky Cypher.[1–3] Current technology development, mainly in the areas of automatic control and navigation, power plants, and composite materials, has overcome the technical problems responsible for the poor success of early vehicles.

Unlike former flying platforms based on thrust deflection, such as the VZ-9V Avrocar circular-wing aircraft,[4] where the flow from a large fan located in the upper center of the machine was ducted to a combination of anular nozzles and peripheral jets to generate lift and control forces, the Cypher aircraft tilting-type vehicle is basically made of a coaxial, counter-rotating bearingless rotor system shrouded by a doughnut-shaped airframe. It uses collective and cyclic blade pitch variation to control rotor thrust and tilting moment, respectively. In some respects, the Cypher concept dates back to the Hiller flying platform, designated VZ-1, which the pilot flew by so-called kinesthetic control, that is, leaning in the desired direction to tilt the aircraft.[4]

The shrouded-rotor design is probably the most distinctive feature of the Cypher machine from the point of view of performance and handling qualities. In fact, the vehicle is still raising interest since the first untethered flight in 1992, due to the high efficiency in hovering and the favorable safety characteristics,[2] where the fuselage envelops and protects the rotors. On the other hand, the axial symmetry of the aircraft, which provides fast and accurate pointing capability, prevents the use of stabilizing surfaces, the effect of which would be highly beneficial in forward flight.

Cypher has proven its value as a maneuverable, controllable, and safe to operate sensor platform, capable of autonomous flight in a

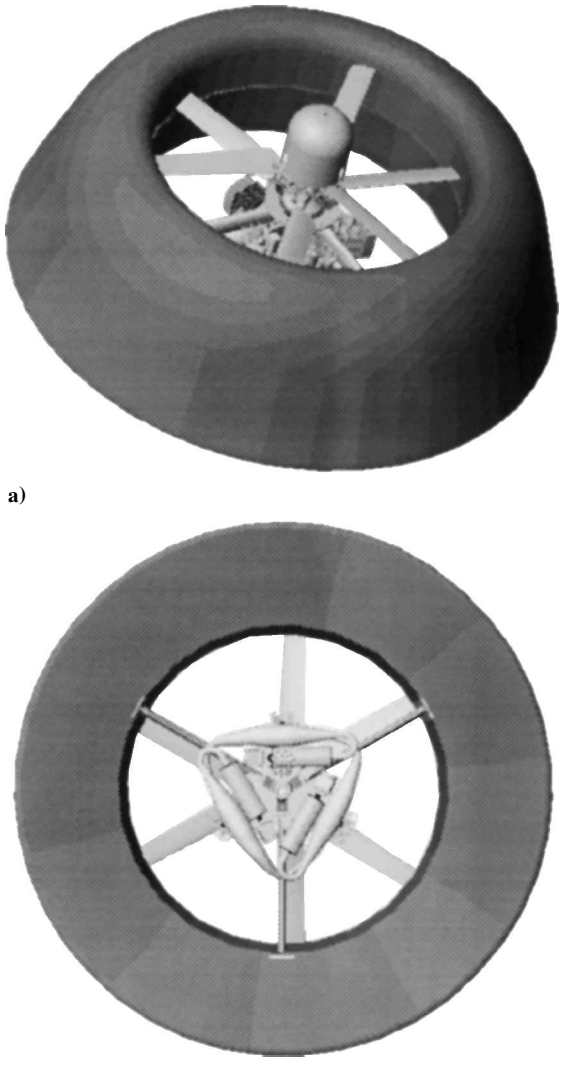

Fig. 1 UAV: a) lateral view and b) view from below.

variety of missions including surveillance, reconnaissance, payload deployment, and geophysical survey.[3] The aerial platform features an advanced flight control system and integrated avionics to accomplish plant stabilization and control and, at a higher level, highly automated management of mission execution.[2]

Thus far, to the authors' knowledge, a complete investigation of the flight mechanics of this kind of shrouded-rotor vertical takeoff and landing (VTOL) platform has not been reported in the literature. The vehicle configuration is rather unconventional, and such aspects as the strong interaction between rotor flow and the aerodynamic field on the fuselage, the inherent instability of the platform, and the significant variation of the aerodynamic derivatives with flight speed are worth detailed study.

This study is dedicated to the analysis of rotor and shroud trim states and dynamic behavior of the shrouded-fan UAV model in Fig. 1. The principal objectives are to identify and interpret key technical and operational aspects of this innovative design, to gain better understanding of its flight capabilities, improve the effectiveness of design process through accurate performance prediction, and set up a sound basis for control system design. To this end, once the vehicle mathematical model is formulated, trim and small-perturbation stability analyses are carried out by classic methods.

The VTOL machine, the characteristics of which are significantly different from those of Cypher, has a maximum takeoff weight of 900 N and is made of a toroidal airframe with a diameter of 1.7 m and a central hub with two counter-rotating, three-bladed rotors, the diameter of which is 1.0 m, equal to the internal diameter of the shroud. The rotors are driven by three two-stroke, air-cooled, one-cylinder engines located in the lower section of the hub. The engines have an overall power of 31 kW at 11,000 rpm and drive three power generators for a total output of 1 kW. The vehicle has one-engine-out flight capability and the payload, for a maximum weight of 100 N, is located in the fuselage.

Because extensive wind-tunnel testing of a powered model or the vehicle itself was ruled out by tight budget constraints, a low-order boundary element code,[5] which includes a boundary-layer analysis, is adopted for flowfield analysis on the airframe. In Ref. 6, the effectiveness of the computer program VSAERO in subsonic inlet design of a vertical/short takeoff and landing (V/STOL) aircraft in transition flight, that is, the capability of predicting flowfields approaching the engine inlet and boundary-layers separation regions for large variation of angle of attack and engine mass flow, was demonstrated by comparison with experimental results. Also, in Ref. 7, a detailed analysis of the coupled rotor-airframe behavior for a tilt-rotor configuration in helicopter mode, from hovering to forward flight, was carried out using the same method. To account for aerodynamic interaction between rotors, wing, and fuselage, rotor wakes, modeled by vortex sheets departing from the appropriate shedding lines, are relaxed to their force-free location in the stream. The present configuration shares some analogy with tilting nacelle/rotor aerodynamic characteristics, and, therefore, the computational code is considered suitable, in this stage of the design process and until more accurate data become available from flight testing, for preliminary solution of the complex aerodynamic field induced by shrouded rotors, as well as for performance analysis and optimization. The latter can be realized by tailoring the airframe through the shaping of the external shroud.

The mathematical model of the UAV is used for trim analysis, where the performance characteristics are determined as a function of speed in terms of actuator angles, attitude angles and required power, among others. These results have been used for rotor blade control system design and engine selection and for mission specification definition.

Next, system stability is investigated to analyze the dynamic behavior of the platform. In so doing, the eigenstructure of the linearized model is calculated, and the effect of flight speed on the vehicle modes is dealt with. Consideration is also paid to such aspects as coupling between longitudinal and lateral-directional modes and timescale separation, which are of interest for the design of a stability augmentation system.

In the same context, due to the aforementioned complexity in the vehicle flowfield and the relevant approximations in the numerical evaluation of the aerodynamic database, the effect of parameter uncertainty on the open-loop stability of the UAV model is determined as a first step for the definition of an uncertainty model to describe the errors due to the variation in the linearized plant dynamics as the steady-state operating point is varied. To this end, sets of derivatives are identified, the perturbation of which affects to a significant extent the system eigenvalues. A robust control technique[8] is envisioned for providing vehicle stabilization and disturbance rejection because the robust controller synthesis process allows explicit consideration of the effect of model uncertainty to obtain a robust stabilization of the vehicle, even in the presence of sizable model errors.

In what follows, the vehicle model is briefly outlined in Sec. II, where the main features of the aerodynamic model are also presented. The obtained results in terms of trim and stability analysis are discussed in Secs. III and IV. A Conclusions section ends the paper.

II. Vehicle Model

The six-degree-of-freedom equations of motion of the vehicle model, for flat-Earth and zero ambient wind, are as follows:

$$\dot{\boldsymbol{v}}_c = -\tilde{\boldsymbol{\omega}}\boldsymbol{v}_c + \frac{1}{m}\begin{bmatrix} X \\ Y \\ Z \end{bmatrix} + \boldsymbol{L}_{BI}\begin{bmatrix} 0 \\ 0 \\ g \end{bmatrix} \tag{1}$$

where $\boldsymbol{L}_{BI}$ is the transformation matrix from inertial to body frame, and

$$\dot{\boldsymbol{\omega}} = \begin{bmatrix} (A_p J_z + A_r J_{xz}) / (J_x J_z - J_{xz}^2) \\ [J_{xz}(r^2 - p^2) + (J_z - J_x) pr + M] / J_y \\ (A_r J_x + A_p J_{xz}) / (J_x J_z - J_{xz}^2) \end{bmatrix} \tag{2}$$

where

$$A_p = J_{xz} pq + (J_y - J_z) qr + L$$

$$A_r = -J_{xz} qr + (J_x - J_y) pq + N$$

and, for the Euler angles, we have the classic form[9] $\dot{\boldsymbol{\Phi}} = \mathcal{E}\boldsymbol{\omega}$.

The forces, X, Y, and Z, and moments, L, M, and N, in Eqs. (1) and (2) are in the body-fixed frame and depend on the density ρ, the linear and angular velocity components $\boldsymbol{v}_c = (u, v, w)^T$ and $\boldsymbol{\omega} = (p, q, r)^T$, respectively, and the control vector $\boldsymbol{u} = (\delta_A, \delta_B, \delta_C, \delta_P)^T$. The state vector is defined as $\boldsymbol{x} = (\boldsymbol{v}_c, \boldsymbol{\Phi}, \boldsymbol{\omega})^T \in \mathcal{R}$.[9] Next, we have

$$\begin{bmatrix} X \\ Y \\ Z \end{bmatrix} = \boldsymbol{F}_R + \boldsymbol{F}_A, \qquad \begin{bmatrix} L \\ M \\ N \end{bmatrix} = \boldsymbol{G}_R + \boldsymbol{G}_A \tag{3}$$

where the subscripts R and A indicate, respectively, rotors and airframe.

Rotor speed $\Omega = 3100$ rpm is kept constant by a rpm governor. The rotors are rigid, that is, not flapping, and the blade pitch is controlled by an arrangement of two mechanically linked swash plates. Pitch and roll controls are obtained by longitudinal, δ_B, and lateral, δ_A, change of blade pitch, whereas yaw control is provided by variation, δ_P, of collective pitch on the lower rotor to unbalance the rotor torque. Note that the latter control action introduces a small coupling between vertical and yaw axes together with the advantage of some mechanical simplicity.

Each rotor has three 0.5 m long blades configured with a NACA 0012 airfoil, linearly tapered with 10 deg linear twist and 0.1 m maximum chord. According to the so-called level-1 modeling,[10] where the rotor loads are determined by analytical integration over blade span, we assume steady-state aerodynamics for the rotors, assume a nonuniform inflow with quasi-steady dynamics, and neglect the interaction between the two rotors in term of induced velocity. In spite of the low blade span (and aspect ratio) in comparison with the helicopter, the blade-tip losses are not considered as a result of the end-plate effect of the duct wall. Finally, the effect of the fuselage on rotor inflow is not accounted for, and the tangential velocity induced by the counter-rotating rotors is assumed zero.

For the rotor force and moment, we write $\boldsymbol{F}_R = \boldsymbol{F}_u + \boldsymbol{F}_l$ and $\boldsymbol{G}_R = \boldsymbol{G}_u + \boldsymbol{G}_l + \tilde{\boldsymbol{r}}_u \boldsymbol{F}_u + \tilde{\boldsymbol{r}}_l \boldsymbol{F}_l$, where u and l refer to the upper and lower rotor, respectively, $\boldsymbol{r}$ is the position vector of the rotor hub center, relative to the c.g., and

$$\boldsymbol{F}_{l/u} = -\rho\pi\Omega^2 R^4 \begin{bmatrix} C_{H_{l/u}} \\ C_{Y_{l/u}} \\ C_{T_{l/u}} \end{bmatrix} \tag{4}$$

$$\boldsymbol{G}_{l/u} = \rho\pi\Omega^2 R^5 \begin{bmatrix} C_{l_{l/u}} \\ C_{m_{l/u}} \\ C_{Q_{l/u}} \end{bmatrix} \tag{5}$$

Nondimensional coefficients in Eqs. (4) and (5) are expressed as a function of $\boldsymbol{v}_c$, $\boldsymbol{\omega}$, and $\boldsymbol{a}$. The aerodynamic actions on the airframe are given as $\boldsymbol{F}_A = \boldsymbol{L}_{BW}(\alpha, \beta_x)(-D_f, -C_f, -L_f)^T$ and $\boldsymbol{G}_A = \boldsymbol{L}_{BW}(\alpha, \beta_x)\,(l_f, m_f, n_f)^T$, where $\alpha = \tan^{-1}[w/(u^2 + v^2)^{1/2}]$, $\beta_x = \tan^{-1}(v/u)$, and $\boldsymbol{L}_{BW}$ is the transformation matrix from wind to body axes. To express $\boldsymbol{F}_A$ and $\boldsymbol{G}_A$, we take advantage of the axial symmetry of the fuselage so that $C_f = l_f = n_f = 0$, and we write

$$L_f = F_f C_l, \qquad D_f = F_f C_d, \qquad m_f = F_f d_f C_m \tag{6}$$

where d_f is the fuselage diameter and

$$F_f = \tfrac{1}{2}\rho V_f^2 S_f, \qquad S_f = \pi d_f^2 / 4$$

$$V_f = \left[u^2 + v^2 + \left(v_{i_0} - w\right)^2\right]^{\frac{1}{2}}$$

being v_{i_0} the uniform component of the induced velocity at middistance between the two rotor disks.

A database was developed for the aerodynamic coefficients due to the airframe using the boundary element code VSAERO by Analytical Methods, Inc.,[5] which includes a propeller-slipstream modeling capability, a wake-relaxation iterative scheme, and integral boundary-layer methods for the evaluation of viscous drag, boundary-layer displacement effects, and separation boundaries. The rotor wake is represented by a vortex sheet, where the inflow velocity is determined by a simple segmented actuator disk approach and momentum theory as a function of $k = |\boldsymbol{v}_c|/(v_{i_0} - w)$. In particular, the rotors are modeled as a single thin actuator disk, no swirl is applied within the slipstream, and the effect of cyclic blade pitch on the induced flow through the duct is not accounted for. To provide interference effects of the slipstream on the airframe and rotor wakes, the wake trajectory is computed by a wake-relaxation procedure once an initial shape is assumed, where the wake strength is determined by the requirements of momentum theory.[7]

Streamline/boundary-layer calculations predict, in forward flight, a separation region in the aft portion of the body and provide information on the position of the wake-shedding panels in the flow separation model.

Unfortunately, as we said, no test data were available to compare the results that will be presented in the next paragraphs. Nevertheless, wind-tunnel data for a subscale model of the shroud alone, without the presence of rotors, showed good agreement with the results of the aerodynamic code, in terms of prediction of separation boundaries and global forces and moments, at values of angle of attack in the range $0 \le \alpha \le -90$ deg. Also, test data allowed assessment of the length of the closed wake used for the modelization of the separated flow region. Body wake length has a significant effect on the estimated drag coefficient of the vehicle.

The viscous drag is determined for a Reynolds number of 2×10^6. Because rotary derivatives are also computed, we have C_l, C_d, and C_m expressed, in tabular form, as functions of α, k, and ω. For instance, the pitch moment coefficient is written as

$$C_m = C_{m_0}(\alpha, k) + C_{m_q}(\alpha, k) q (d_f / 2V_f) \tag{7}$$

Because it can be demonstrated that, in potential flow calculations, the flowfield depends on two parameters only, namely, the angle of attack α and k, the aerodynamic coefficients, computed for the purpose of trim and stability analysis, are reported in Fig. 2 as functions of k for $\omega = 0$ and three ranges of angle of attack, namely, $-20 \le \alpha \le 0$ deg (Fig. 2a), $-90 \le \alpha \le -80$ deg (Fig. 2b), and $80 \le \alpha \le 90$ deg (Fig. 2c), which correspond to cruise conditions at small flight-path angle, nearly vertical descending flight, and climbing flight, respectively.

Focusing on the influence of speed in forward flight ($-20 < \alpha \le 0$), we have that the effects of rotor inflow are reduced at higher α. Therefore, we see in Fig. 2 that, at low k, the drag coefficient is negative and increasing in modulus for smaller α, due to the suction on the inlet lip. At higher values of k, coefficient C_d becomes positive because of the parasite drag of the airframe. In this situation, C_d grows at smaller (negative) angle of attack due to the increasing induced drag and projected frontal area of the vehicle.

In the same range of variation of α, the lift coefficient exhibits a relevant reduction at both decreasing angle of attack, because the airframe behaves as a lifting surface at negative incidence, and increasing k. In the latter case, the already cited effect of rotor inflow at the inlet lip is greatly attenuated. The high efficiency of the configuration in hovering can be interpreted when we observe the large, positive value of C_l developed at very small α and k.

Next, the plot of pitch coefficient ($-20 \le \alpha \le 0$ deg, $k > 0$) shows that for very small values of k, coefficient C_m approaches zero as

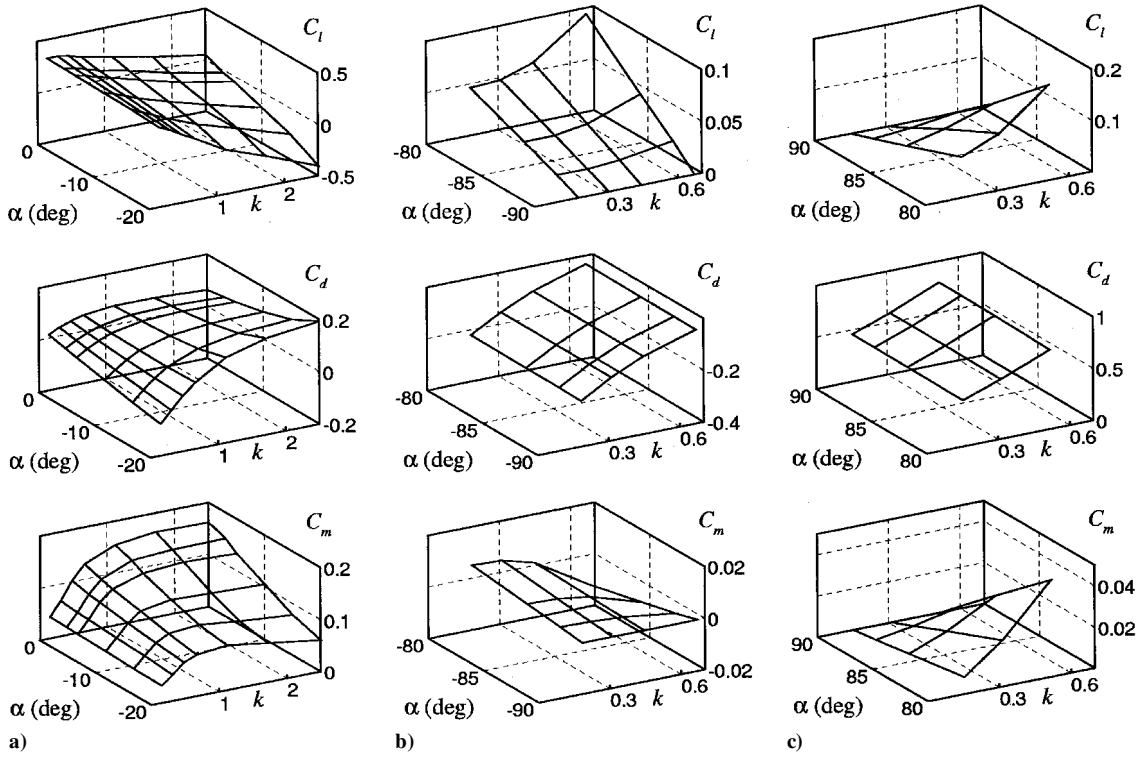

Fig. 2 Force and moment coefficients vs α and k.

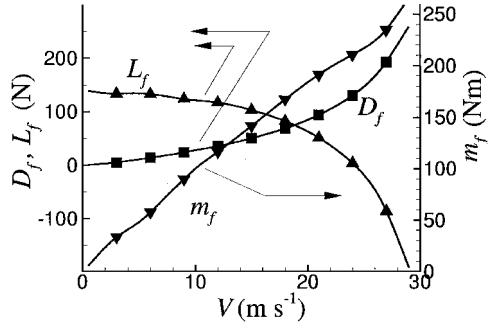

Fig. 3 Airframe force and moment components at trim vs forward speed.

Table 1 Design parameters

Parameter	Value
d_f, m	1.73
R, m	0.55
$\boldsymbol{r}_l$, m	$(0, 0, -0.16)^T$
$\boldsymbol{r}_u$, m	$(0, 0, -0.26)^T$
m, kg	78.0
J_x, kg · m^2	7.1
J_y, kg · m^2	7.1
J_z, kg · m^2	12.6
J_{xz}, kg · m^2	0

expected, regardless of the angle of attack, whereas positive, nose-up values of C_m result when the flight speed is increased. In particular, high values of local velocity in the forward zone of the inlet lip are responsible for the significant nose-up tendency of the vehicle in forward flight. At constant k, the pitch coefficient decreases with α because a nonnegligible suction force is also experienced in the lower, upstream region of the shroud, and C_m is also reduced as k is larger, when the induced flow on the inlet lip is low in comparison with the external flow velocity. This latter situation is typical in shrouded fan configurations where the duct height over diameter ratio is low,[11] as in the present airframe having a 0.6 m height.

Turning to the computed coefficients for flight conditions at large positive or negative flight-path angle, shown in Figs. 2b and 2c, respectively, we see very low values of C_m, because the flowfield is nearly axisymmetric and, again, the significant effect of the shroud in term of lifting force in the plots of drag coefficient at $\alpha = \pm 90$ deg.

As for the hovering flight, represented by $k = 0$, we have the development of a favorable suction on the inlet lip, the effect of which is expressed through the normal force in body axes $Z_A = -0.34 F_f$. Correlation between hovering and other flight conditions in the database is accomplished through linear interpolation.

III. Trim Analysis

The trim problem is formulated and solved as a minimization problem with specified constraints.[9] We consider level and straight flight conditions at speed in the range $0 \leq V \leq 30$ ms^{-1}. Geometric and inertial parameter of the considered configuration are reported in Table 1.

Airframe lift and drag force together with pitch moment are shown, at trim, in Fig. 3 as a function of velocity. The performance characteristics of the UAV in forward flight can be interpreted when reference is made to the relevant increment of D_f and the reduction of L_f at increasing speed. This is explained by the rather large pitch-down angle visible in Fig. 4, where $\theta \approx \alpha$ in nearly symmetric flight, because the thrust vector is to be tilted forward at large angles to balance the fuselage drag. Because the drag is significantly affected by the pitch angle, as we said, the equilibrium is realized at an ever decreasing attitude angle. Also, the negative angle of attack (or θ) is responsible for the low, negative value of lift force at high speed.

The airframe moment in Fig. 3 is balanced by the rigid-rotor control moment, generated by longitudinal cyclic pitch. As already mentioned as regards C_m, the nose-up moment on the fuselage exhibits a nearly linear variation with speed. A few data, suitable for comparison with the present results, are available from Ref. 12, where the Cypher trim moment vs speed is discussed. There, the nose-up moment is shown to increase up to 13 m · s^{-1} and then to decrease. The maximum value is about 200 N · m, somewhat comparable with the result in Fig. 3.

Although the origin of the data reported in Ref. 12, that is, theoretical or experimental, was not specified, the discrepancy at high speed can be either due to different shroud geometry because, reportedly,

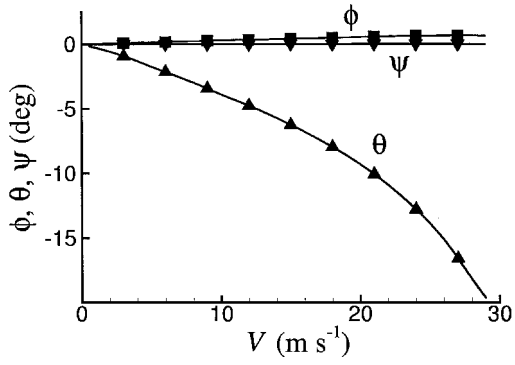

Fig. 4 Roll, ϕ, pitch, θ, and yaw, ψ, angles vs forward speed.

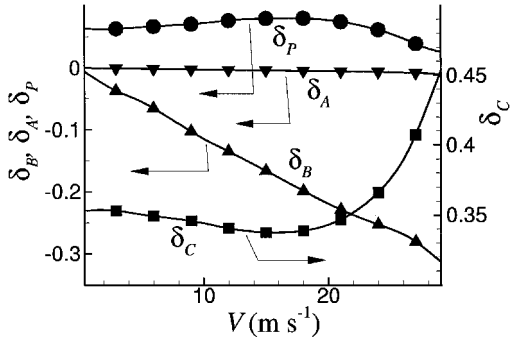

Fig. 5 Control angles vs forward speed.

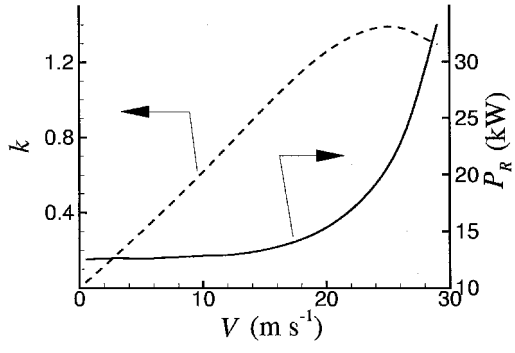

Fig. 6 Required power and k vs forward speed.

the Cypher fuselage was shaped to provide a negative (nose-down) moment, or to some of the aforementioned assumptions. In particular, consideration of the velocity induced by longitudinal blade pitch would reduce the computed m_f due to a more limited inflow in the forward region of the rotor disk. In this respect, we also note that the present results can be regarded as conservative because a lower pitch moment would decrease the required control action.

Figure 4 shows that, in the considered range of forward speed, roll and yaw angles are very small as a result of the counter-rotating rotors, In fact, nonzero values of ϕ are obtained only because differential pitch is realized through a variation of the lower rotor collective only.

Turn to Fig. 5, where the control angles are shown vs forward speed; the collective pitch δ_C exhibits a large and rapid increase at $V > 20\ \mathrm{m \cdot s^{-1}}$ that reveals, as we already observed, the limitations of this kind of configuration in term of maximum achievable velocity in level flight. Figure 5 shows the longitudinal cyclic δ_B, the trend of which is somewhat classic in comparison with the helicopter. Next, very small variations of both δ_A and δ_P are obtained, as expected. In this respect, note that the differential command is required to compensate for small offsets in blade pitch of the two rotors due to slight differences in the geometry of upper and lower swash-plate linkages.

Induced velocity on the two rotors is also expected to be different due to their mutual interaction and, in spite of the small distance between the disks, equal to 10% of the rotor radius. In this respect, we assume that the effect of rotor interference on downwash is dealt with by changing the collective pitch required by each rotor.

The required power at sea level as a function of forward speed is shown in Fig. 6, where we observe that, unlike conventional fixed- or rotary-wing aircraft, the decrease in power required at intermediate speed is practically absent because, due to the nose-down pitch attitude and negative lift, the thrust is to be significantly increased with speed for the balance of vertical force. For the sake of completeness, k at equilibrium is also reported as a function of V. The reduction of this parameter at high speed is explained by considering that both w and v_{i_0} increase with $|\theta|$ and δ_C, respectively.

IV. Stability Analysis

Equations (1–3) were numerically linearized, and a multidimensional curve fit was used to provide a C^1 model for the aerodynamic coefficients. Figures 7 and 8 show the root loci vs speed of the longitudinal and lateral-directional modes, respectively, and allow the stability characteristics of the vehicle to be interpreted. Eigenvalues and eigenvectors of the vehicle in hovering and forward flight at $V = 25\ \mathrm{m \cdot s^{-1}}$ are also reported in Tables 2 and 3, respectively.

Looking first at the dynamics in hovering, we have the one-degree-of-freedom yaw and heave subsidences, the eigenvalues of which are accurately expressed by the N_r and Z_w derivatives, respectively, that is, $\lambda_{\mathrm{yaw}} = -3.0 \times 10^{-2}$ and $\lambda_{\mathrm{heave}} = -4.3 \times 10^{-1}\ \mathrm{s^{-1}}$. Accordingly, the heave time constant is 2.3 s, which, with a blade loading of about $3000\ \mathrm{N/m^2}$, is a somewhat typical value for helicopter. The negative value of the yaw damping derivative is a result of the variation of blade velocity relative to the fluid on the upper and lower rotor torques that, at $V = 0$, can be expressed in concise form as $Q_u = k(\Omega - r)^2$ and $Q_l = -k(\Omega + r)^2$, where k is a constant coefficient. Note that the upper rotor has a counterclockwise rotation direction.

Next, due to the airframe axial symmetry from which it results, in terms of significant aerodynamic derivatives

$$X_u = Y_v, \qquad L_v = -M_u, \qquad L_p = M_q, \qquad M_p = -L_q \quad (8)$$

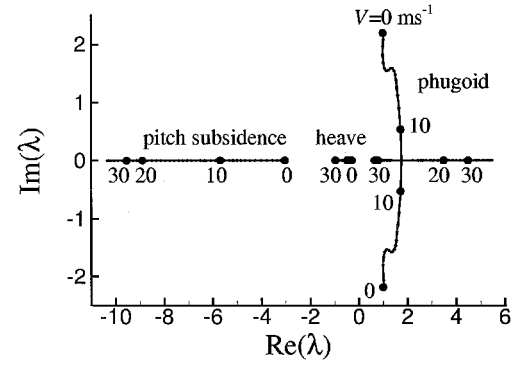

Fig. 7 Loci of longitudinal eigenvalues vs forward speed.

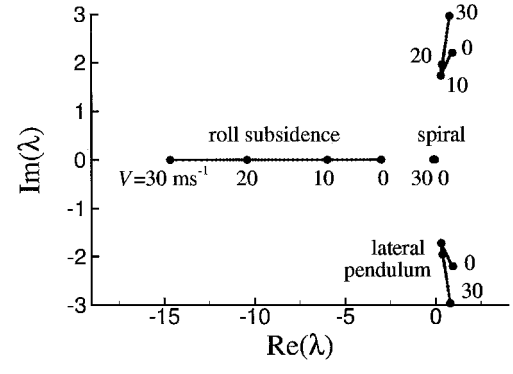

Fig. 8 Loci of lateral eigenvalues vs forward speed.

Table 2 UAV model eigenstructure for $V = 0$

	Longitudinal modes			Lateral-directional modes		
λ	-2.975	$0.961 \pm 2.184i$	-0.878	-2.969	$0.949 \pm 2.184i$	-0.033
u	0.644	$0.734 \pm 0.361i$	0.355	0.344	$0.059 \pm 0.198i$	-0.000
v	-0.345	$0.200 \pm 0.053i$	0.000	-0.646	$0.066 \pm 0.817i$	0.000
w	0.013	$-0.007 \pm 0.026i$	-0.934	0.007	$-0.006 \pm 0.003i$	-0.000
ϕ	0.103	$0.032 \pm 0.039i$	-0.000	0.192	$0.189 \pm 0.068i$	0.000
θ	0.192	$-0.156 \pm 0.127i$	0.023	0.102	$-0.050 \pm 0.007i$	0.000
ψ	0.000	$-0.000 \pm 0.000i$	0.000	0.000	$-0.000 \pm 0.000i$	-1.000
p	-0.306	$-0.054 \pm 0.108i$	0.000	-0.570	$0.329 \pm 0.347i$	0.000
q	-0.571	$0.127 \pm 0.462i$	-0.021	-0.304	$-0.063 \pm 0.103i$	0.000
r	0.000	$0.000 \pm 0.000i$	0.000	0.000	$-0.000 \pm 0.000i$	0.033

Table 3 UAV model eigenstructure at $V = 25\ \mathrm{ms}^{-1}$

	Longitudinal modes				Lateral-directional modes		
λ	-10.228	5.124	0.560	-0.588	-12.121	$0.556 \pm 2.351i$	-0.084
u	-0.233	-0.196	0.626	0.668	-0.003	$0.000 \pm 0.001i$	-0.009
v	-0.011	-0.002	-0.006	-0.005	-0.618	$0.767 \pm 0.622i$	0.013
w	-0.908	-0.950	-0.775	-0.743	-0.012	$-0.002 \pm 0.001i$	-0.000
ϕ	0.001	-0.000	-0.000	0.001	0.063	$0.039 \pm 0.038i$	-0.205
θ	-0.034	-0.046	-0.073	0.022	-0.001	$0.000 \pm 0.000i$	-0.001
ψ	-0.000	-0.000	-0.001	0.000	0.008	$-0.032 \pm 0.013i$	0.975
p	-0.011	-0.001	-0.000	-0.000	-0.779	$-0.079 \pm 0.096i$	-0.003
q	0.346	-0.237	-0.041	-0.013	0.006	$0.000 \pm 0.000i$	-0.001
r	-0.001	0.001	0.000	0.000	-0.089	$-0.046 \pm 0.066i$	-0.080

a couple of unstable motions with virtually coincident characteristics given by $\omega_{n_{1,2}} = 0.66\ \mathrm{rad} \cdot \mathrm{s}^{-1}$ and $\zeta_{1,2} = -0.23$ are associated with oscillations of u, q, and θ and v, p, and ϕ. In both cases, variations of longitudinal states lag the lateral states by 90 deg in phase. Finally, a highly damped mode $\lambda_3 = -1.34 \pm 7.0 \times 10^{-3} i\ \mathrm{rad} \cdot \mathrm{s}^{-1}$ involves, like in the earlier circumstance, all of the states but w and r.

Note that, in hovering, a weak coupling between longitudinal and lateral dynamics is provided by the cross-damping derivatives L_q and M_p, where $M_P = -L_q = 1.1 \times 10^{-2}\ \mathrm{rad} \cdot \mathrm{s}^{-1}$. The nonzero value of these coefficients is due to changes in X and Y forces on the two rotors that generate pitch and roll moments, respectively, because of the different vertical offset of the rotor hubs from the c.g. With reference to conditions (8), X_u and Y_v are related to rotor drag and side force, the shroud contribution being negligible at very low speed. The same X and Y forces are associated to the generation of pitch and roll moments represented by derivatives L_v and M_u. Pitch and roll damping is provided thrust offset from the c.g. caused by w-velocity gradients along x and y axes, respectively, induced by q and p angular rates of the nonflapping rotors.

Longitudinal stability in forward flight is characterized by the effect of M_w derivative, which leads to coupling of translational u and w and rotational q degrees of freedom. Also, the symmetrical structure of longitudinal, u, q, and θ, and lateral, v, p, and ϕ, dynamic subsystems provided by Eqs. (8) is not retained so that, already at low speed, system eigenstructure shows the expected uncoupling between longitudinal and lateral modes. In particular, at low and moderate speed, longitudinal motion is composed of a couple of subsidences that will be referred to as pitch and heave modes, in analogy with a conventional helicopter, and an unstable phugoid mode. The pitch subsidence involves pitch attitude together with u and w, whereas, in the heave subsidence, angular motion is practically absent and w and, to a lesser extent, u translational velocities are excited. The unstable phugoid motion involves all of the longitudinal states, and its frequency decreases at growing speed, a frequent situation in helicopter dynamics. For $V > 15\ \mathrm{m} \cdot \mathrm{s}^{-1}$ the phugoid degenerates into two exponential modes that remain unstable up to the maximum level velocity.

Turning to the lateral-directional dynamics in forward flight (Fig. 8), we have a lightly damped yaw (spiral) subsidence due to the very low value of the yaw damping derivative in the absence of vertical empennage, a lateral pendulum motion, and a roll subsidence. The damping of the roll subsidence is increased almost by a factor five from $V = 1\ \mathrm{m} \cdot \mathrm{s}^{-1}$ to maximum velocity, whereas, in the same speed range, the time to half of the pitch subsidence is reduced by a factor three.

The shroud provides a significant effect on the stability through the moment derivatives M_u, L_v, and M_w, together with some positive damping, that is, a negative contribution to L_p and M_q. The speed derivatives are slightly influenced by flight speed because the effect of dynamic pressure is balanced by the reduction of trim moment coefficient that results from the decrement of α when the vehicle is trimmed at increasing forward velocity. The same argument applies to L_v, where a negative rolling moment is generated by positive lateral speed. In a similar fashion, the variation of M_w with speed is small, and the incidence stability derivative is greater than zero because, with $\alpha < 0$ at trim, a reduction in module of the angle of attack gives rise larger values of tangential velocity on the forward lip of the shroud. Finally, as we said, the airframe contribution to the Z force is not negligible, and therefore, we have $Z_w < 0$, which represents the positive lift curve slope of the shroud in the rotor induced flowfield.

In Table 3 we observe that, as expected because of the axial symmetry and the absence of stabilizing surfaces, and unlike helicopter dynamics, the coupling of longitudinal and lateral-directional modes remains weak as the forward speed is increased. Also, as far as the validity of reduced-order models and, therefore, the understanding of the vehicle behavior is concerned, the separation of slow and fast modes is not possible for this vehicle, at least for the longitudinal dynamics, because of the relatively high frequency of the pendulum mode.

Because of the somewhat gross simplifications involved in the formulation of the aerodynamic model of the vehicle, a simple analysis of the effect of uncertainty in the UAV model on open-loop system stability is performed. To this end, the state matrix of the linearized system is partitioned as follows:

$$\boldsymbol{A} = \begin{bmatrix} \boldsymbol{A}_1 & \boldsymbol{G} & \boldsymbol{A}_2 & \boldsymbol{B}_1 \\ 0 & 0 & \boldsymbol{C} & 0 \\ \boldsymbol{A}_3 & 0 & \boldsymbol{A}_4 & \boldsymbol{B}_2 \\ 0 & 0 & 0 & \boldsymbol{D} \end{bmatrix} \tag{9}$$

where $\boldsymbol{G}$ represents gravity effects, $\boldsymbol{C}$ depends on attitude kinematics, $\boldsymbol{B}_1$ and $\boldsymbol{B}_2$ give the effects of actuator positions on linear and

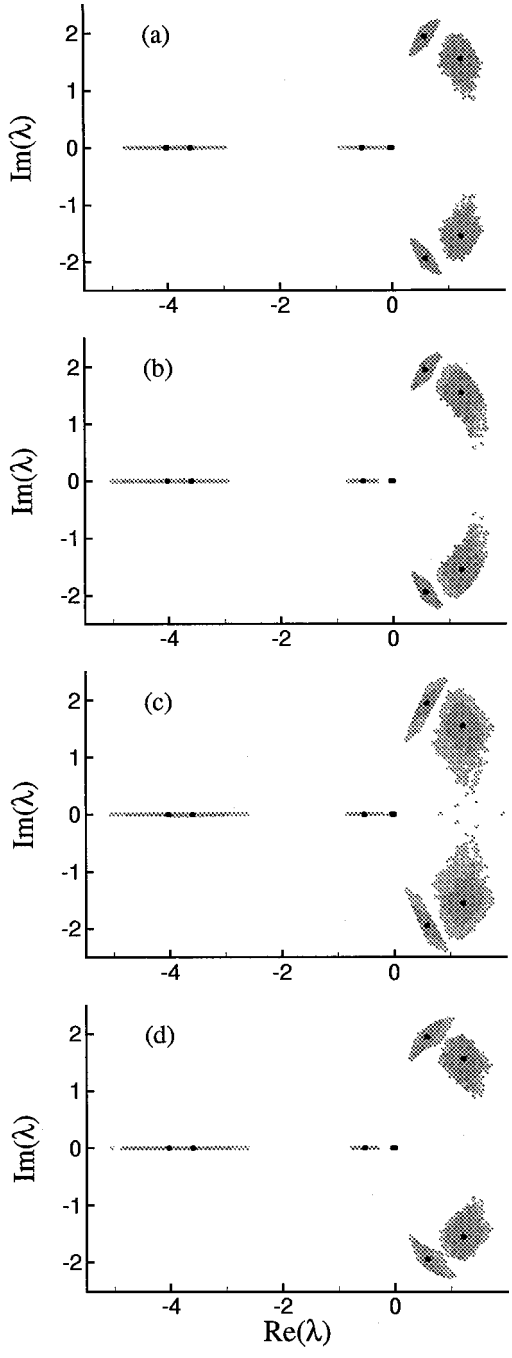

Fig. 9 Open-loop pole uncertainties: $V = 5$ m · s^{-1}.

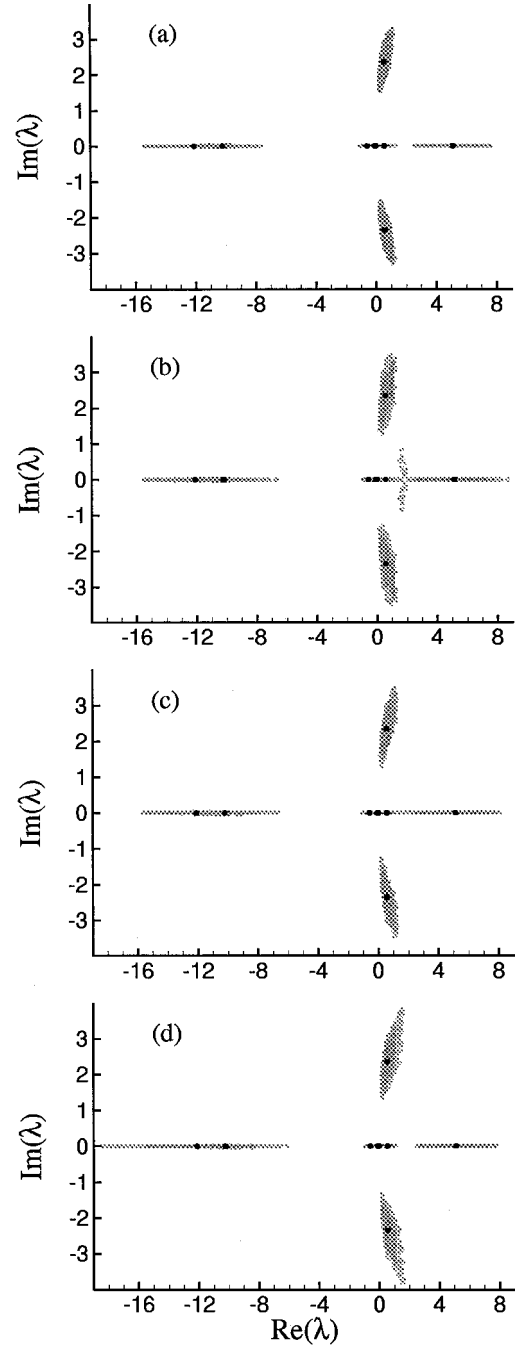

Fig. 10 Open-loop pole uncertainties: $V = 25$ m · s^{-1}.

angular accelerations, respectively, $\boldsymbol{D} = -\text{diag}\{1/\tau_1, \ldots, 1/\tau_6\}$, and $\boldsymbol{A}_i$, $i = 1, \ldots, 4$, depends on aerodynamic derivatives. Our objective is to determine the variations induced in the eigenvalues by matrix perturbations $\Delta\boldsymbol{A}_i$ and, consequently, to identify those sets of derivatives, each corresponding to one of the $\boldsymbol{A}_i$ that have a larger effect on the open-loop stability. This approach could be regarded as a first step in the formulation of a uncertainty model for the design of a robust controller. The matrices $\Delta\boldsymbol{A}_i$ are obtained by random perturbation of the elements of $\boldsymbol{A}_i$ that depend on aerodynamic derivatives, up to a given percentage P of their nominal value.

The scatter plots of poles, provided in Figs. 9 and 10 for $V = 5$ and 25 m · s^{-1}, respectively, are traced for 1000 sets of random perturbations on matrices $\boldsymbol{A}_i$. In Figs. 9 and 10, black dots represent the eigenvalues of $\boldsymbol{A}$, omitting the poles associated to actuator dynamics, in the nominal condition $P = 0$. Next, the areas shaded in dark gray give the loci obtained for a perturbation corresponding to $P = 0.3$ on all of the $\boldsymbol{A}_i$. Finally, the effect of perturbing different groups of derivatives is provided by the light gray regions traced, in Figs. 9a–9d (and Figs. 10a–10d) for a 60% variation of $\boldsymbol{A}_i$, $i = 1, \ldots, 4$, respectively.

In Fig. 9a we observe that perturbations of $\boldsymbol{A}_1$, that is, the force derivatives with respect to velocity components, have a limited effect on the stability, whereas in Figs. 9b and 9d, we have that $\Delta\boldsymbol{A}_2$ and $\Delta\boldsymbol{A}_4$, representing variations of force and moment derivatives, respectively, with respect to angular velocity components, have a major influence on the two subsidences, as expected. More important, it appears from Fig. 9c that the two unstable, pendulum motions are extremely sensitive to the moment derivatives with respect to angular velocity $\boldsymbol{A}_3$. This aspect is relevant because it confirms that an accurate modeling of the aerodynamic moment is to be realized for a successful stabilization of the system.

Similar conclusions can be drawn from Fig. 10, where a larger sensitivity of the subsidences to $\Delta\boldsymbol{A}_4$ is apparent (Fig. 10d). This represents a minor problem because of the high stability of these motions. Again, uncertainties on $\boldsymbol{A}_4$ (Fig. 10d) and, to a lesser extent, $\boldsymbol{A}_2$ (Fig. 10b) have a relevant influence on the periodic motion,

whereas large variations of the characteristics of the unstable aperiodic mode are caused by ΔA_3 (Fig. 10c).

A final observation concerns the effects of uncertainty in hovering. This situation is not illustrated by a figure because the eigestructure is much more robust to parameter perturbation than in the earlier cases. The effects of A_2 and A_4 are negligible, due to the low value of the related aerodynamic derivatives at $V = 0$. The heave mode and the coinciding longitudinal and lateral-directional pendulum motions present a mild sensitivity to ΔA_1 and ΔA_3, respectively.

V. Conclusions

The principal objectives of this study were performance and stability analyses of a novel UAV model. The results are used in the vehicle design and development process.

The aerodynamic analysis allows for the realization of a database suitable for trim and performance evaluation. Unfavorable characteristics of the vehicle are the large drag force due to the nose-down pitch attitude required for forward flight and, more important, a nose-up moment developed by the airframe the value of which is ever increasing with speed. On the other hand, the high efficiency in hovering of the shrouded-rotor configuration is confirmed by our analysis.

The dynamic behavior of the model is characterized by unstable pendulum modes for both longitudinal and lateral-directional degrees of freedom in almost the whole operating speed range of the vehicle. Coupling of longitudinal and lateral-directional dynamics remains low at any speed due to the vehicle geometry and the effect of counter-rotating rotors. Timescale separation of slow and fast dynamics is not possible due to the high frequency of the periodic modes.

As a final observation, the results of uncertainty analysis indicate that the moment derivatives with respect to angular velocity components have a crucial effect on the system stability. Therefore, a more accurate evaluation of these terms should be conducted by wind-tunnel testing of a powered configuration.

Acknowledgments

This work was partially supported by the National Program of Researches in Antarctica and the Italian Ministry of University and Scientific Research.

References

[1]Cycon, J. P., "Decoding the Cypher UAV," *Vertiflite*, Vol. 36, No. 6, 1990, pp. 56–58.

[2]Thornberg, C. A., and Cycon, J. P., "Sikorsky Aircraft's Unmanned Aerial Vehicle, Cypher: System Description and Program Accomplishments," *Proceedings of the Annual Helicopter Society 51st Annual Forum*, Fort Worth, TX, May 1995, pp. 804–811.

[3]Walsh, D., and Cycon, J. P., "The Sikorsky Cypher UAV: A Multi-Purpose Platform with Demonstrated Mission Flexibility," *Proceedings of the Annual Helicopter Society 54th Annual Forum*, Washington, DC, May 1998, pp. 1410–1418.

[4]Campbell, J. P., *Vertical Takeoff and Landing Aircraft*, Macmillan, New York, 1962, Chap. 7.

[5]Clark, D.R., Maskew, B., and Dvorak, F. A., "The Application of a Second Generation Low-Order Panel Method Program VSAERO to Powerplant Installation Studies," AIAA Paper 84-0122, 22nd Aerospace Sciences Meeting, Reno, NV, Jan. 1984.

[6]Tindell, R., and Potonides, H., "Substantiation of the Applicability of VSAERO Panel Method to Subsonic Inlet Design," AIAA Paper 85-1119, AIAA/SAE/ASME 21st Joint Propulsion Conf., Monterey, CA, July 1985.

[7]Clark, D. R., and McVeigh, M. A., "Analysis of the Wake Dynamics of a Typical Tilt-Rotor Configuration in Transition Flight," 11th European Rotorcraft Forum, Paper 29, Sept. 1985.

[8]Skogestad, S., and Postlethwaite, I., *Multivariable Feedback Control: Analysis and Design*, Wiley, New York, 1996, Chap. 2.

[9]Stevens, B. L., and Lewis, F. L., *Aircraft Control and Simulation*, Wiley, New York, 1992, Chap. 3.

[10]Padfield, G. D., *Helicopter Flight Dynamics: The Theory and Application of Flying Qualities and Simulation Modeling*, Blackwell Science, Oxford, UK, 1996, Chap. 3.

[11]Lazareff, M., "Aerodynamics of Shrouded Propellers," *The Aerodynamics of V/STOL Aircraft*, AGARDograph 126, May 1968, pp. 237–289.

[12]Cycon, J. P., "Sikorsky Aircraft UAV Program," *Vertiflite*, Vol. 38, No. 3, 1992, pp. 26–30.